Image Anal Stereol 2025;44:87-95 doi: 105566/ias.3442
Original Research Paper

CEREBROVASCULAR ATLAS FROM MRA IMAGING OF 1336 SUBJECTS

XINYU WANG[1], JIALU LIU[2,3], XIAOPING LOU[✉,1]

[1] Key Laboratory of The Ministry of Education for Optoelectronic Measurement Technology and Instrument, Beijing Information Science and Technology University, Beijing 100192, China; [2] Laboratory of Brain Atlas and Brain-inspired Intelligence, Institute of Automation, Chinese Academy of Sciences, Beijing, China; [3] School of Artificial Intelligence, University of Chinese Academy of Sciences, Beijing, China
e-mail: wangxinyu2022@bistu.edu.cn; liujialu2023@ia.ac.cn; louxiaoping@bistu.edu.cn
(Received November 7, 2024; revised March 17, 2025; accepted March 17, 2025)

ABSTRACT

This study aimed to create a comprehensive statistical atlas of cerebral arteries to accurately capture variations among individuals and across different age groups. We utilized 1,336 publicly available multicenter magnetic resonance angiography (MRA) and T1-weighted MRI datasets, employing an automated blood vessel segmentation method, FFCM-MRF, to segment all blood vessels and measure their radii. Subsequently, the binary segmentation and vascular radius images were nonlinearly registered to the Montreal Neurological Institute (MNI) brain template using the T1-weighted MRI dataset. This process resulted in the creation of atlases that illustrate the probability of arterial occurrence, the average arterial radius, and the standard deviation of the arterial radius. The constructed vascular statistical atlas effectively showcases the major arteries and, when integrated with the probability atlas and the average vessel radius atlas, indicates a significantly higher probability of larger arteries, which decreases as the vessel radius diminishes. This observation aligns with previous research findings, and the similarity between the probability atlas and individual vascular images reached as high as 0.9659. In conclusion, this atlas effectively covers arterial radius information across nearly the entire age range, enabling the identification of variations between individual arterial voxel radii and the population using this atlas, thereby providing an important reference for cerebral vascular research.

Keywords: Angiography, Cerebral vessels, Magnetic resonance imaging, statistical atlas.

INTRODUCTION

The brain is the central organ of the nervous system in humans and all vertebrates, and it is characterized by one of the most intricate tissue structures. Neuronal computation within the brain requires a substantial and continuous supply of energy, making it highly dependent on the vascular system for the continuous transport of nutrients and oxygen.

Changes in cerebrovascular structure are critical factors that influence various brain diseases. Common cerebrovascular disorders in humans include conditions such as cerebral arteriosclerosis, cerebrovascular stenosis, cerebral infarction, and aneurysms. Studies have shown that defects in the vascular network of the central nervous system are associated with early symptoms of neurodegenerative diseases, such as Alzheimer's disease and amyotrophic lateral sclerosis (ALS) (Iadecola *et al.*, 2018). Therefore, gaining a comprehensive understanding of the normal morphology and distribution of cerebral arteries is essential for improving disease detection.

Currently, most brain atlas studies primarily focus on representing and describing tissue types, as well as anatomical and functional brain regions. There is a notable lack of research on the morphology and distribution of cerebral arteries. Developing a cerebral artery atlas could help establish standard data for healthy individuals and facilitate the early detection of cerebrovascular abnormalities. In this study, we refer to the "statistical atlas" as a comprehensive representation of cerebrovascular structures, which includes both the vascular probability atlas (depicting the spatial distribution of vessels) and other statistical measures such as vessel radius distribution. A vascular probability atlas specifically highlights the likelihood of vessel presence in different regions, while the statistical atlas encompasses additional quantitative features to provide a more holistic view of cerebrovascular morphology.

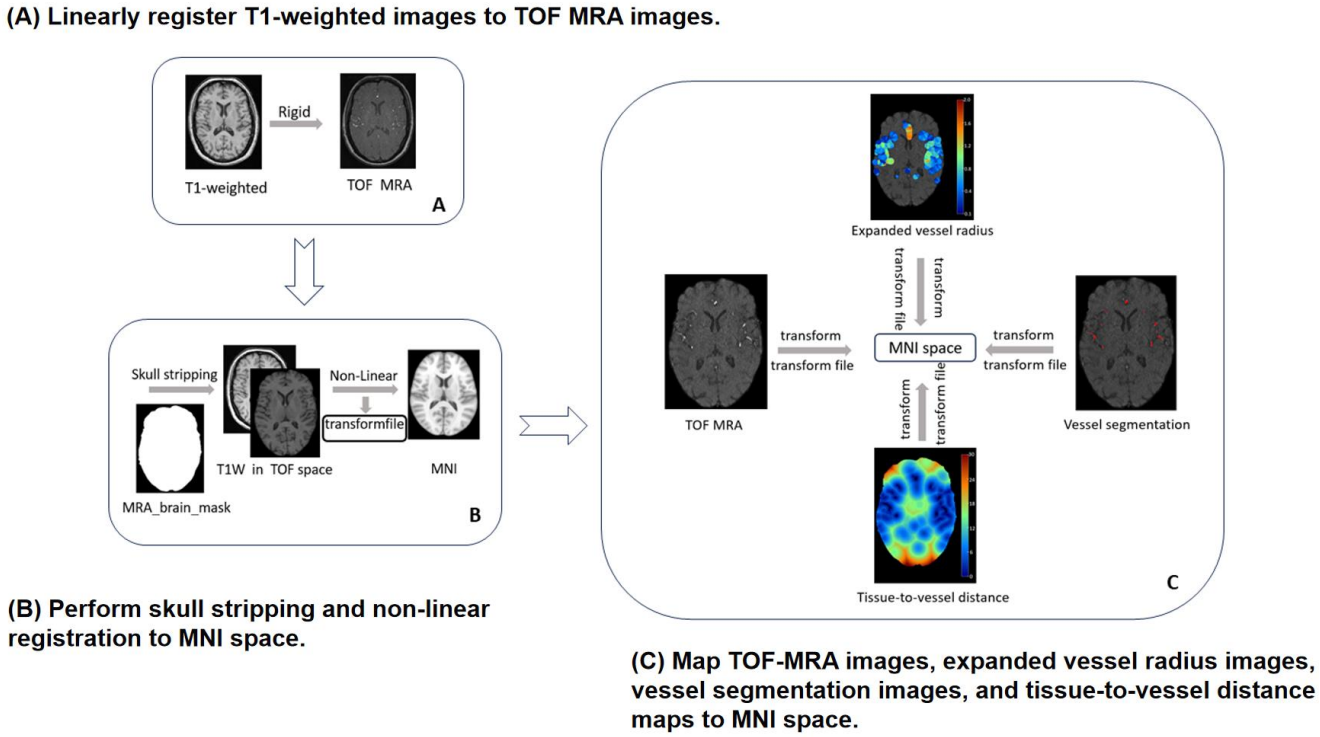

Fig. 1. *Statistical Atlas Generation Image Processing Pipeline*

Previous studies have explored related topics. In 2003, a study constructed a vascular density map with 9 participants (n = 9) (Cool *et al.*, 2003), and in 2011, another study created an arteriovenous map using vascular information from 54 participants (n = 54) (Dufour *et al.*, 2011). However, the limited number of participants in these studies may significantly affect the results due to individual variability. Building on this, a 2013 study employed a dataset of 700 subjects (Forkert *et al.*, 2013); however, it relied solely on linear registration to standard space, which may not accurately align the data. In 2017, another study analyzed 167 MRA images (Dunås *et al.*, 2015), utilizing nonlinear registration to generate a probabilistic vascular map. Nevertheless, the age of the subjects in this study predominantly ranged from 64 to 68 years, which does not adequately represent the vascular structure and distribution across a broader age range. Although some previous vascular statistical atlases have included datasets with a broader age distribution, the sample sizes remain relatively small (Mouches *et al.*, 2019). This work aims to construct a comprehensive statistical arterial atlas using a larger sample size and diverse age groups, thereby providing a more accurate representation of cerebrovascular morphology and capturing individual variability.

Fig. 1 shows a diagram of the image processing pipeline used for this research, which is described in more detail below.

MATERIALS AND METHODS

DATASETS

A total of 1443 datasets from healthy subjects were included. Among them, 78 datasets did not have T1-weighted MRI images, and the remaining datasets included high-resolution T1-weighted MRI and TOF MRA images, which were used to generate a human cerebral artery statistical atlas.

ADAM (https://adam.isi.uu.nl) is a dataset for the 2020 Aneurysm Detection and Segmentation Challenge, with 109 subjects in total, of which only 20 are healthy. The ICBM dataset (https://ida.loni.usc.edu/) has 192 healthy subjects in total, of which 4 were excluded due to lack of clinical information.

The CHUV dataset (https://openneuro.org/datasets/ds003949/versions/1.0.1), obtained from the University Hospital of Lausanne, consists of 284 subjects, including 127 healthy controls and 157 patients with cerebral aneurysms. The BraVa dataset (http://cng.gmu.edu/brava/) includes 56 healthy subjects. The 571

datasets from healthy subjects were downloaded from the IXI database (http://brain-development.org), which combines MRI collections from three different centers in London, UK. In the IXI dataset, all subjects were normal and healthy, and 19 of them were excluded without clinical information. The MIDAS dataset was collected and provided by CASILab at the University of North Carolina at Chapel Hill (UNC) and distributed by the MIDAS data server of Kitware, Inc.(http://insight-journal.org/MIDAS/community/view/21). A total of 109 subjects were included. Ten subjects were excluded due to a lack of clinical data, and another seven UNC subjects were excluded due to incidental findings (such as ethmoid sinus polyps, micro-intubated acoustic tumors, epidermoid cysts, and micro-strokes). The MSC dataset (https://openneuro.org/datasets/ds000224/versions/1.0.3) includes scans of 10 subjects, each scanned four times, and we selected the results of one scan. OASIS3 (https://www.oasis-brains.org) is a longitudinal multimodal dataset that includes neuroimaging, clinical, cognitive, and biomarker data for normal aging and Alzheimer's disease. A total of 359 healthy subjects were included.

Table 1. *Demographic information of the finally included subjects.*

Center	n	Sex		Mean Age(range)
		M	F	
ADAM	20			
ICBM	174	73	101	42(19-80)
CHUV	106			
BraVa	56	21	35	31(19-64)
IXI-HH	176	86	90	47(20-82)
IXI-IOP	58	20	38	43(21-86)
IXI-Guys	294	128	166	50(20-86)
MIDAS	92	42	50	42(19-72)
MSC	10	5	5	29(24-34)
OASIS3	350			69(42-92)

Table 2. *TOF MRA acquisition parameters*

Center	Scanner	Magnetic field strength(T)	Voxel resolution (mm^3)	TR/TE (ms)	Flip angle (degrees)
ADAM	Philips	1.5/3	0.3571×0.3571×0.5000/ 0.3906×0.3906×0.5000	22/3.45	
ICBM	Siemens	1.5/3	0.6250×0.6250×0.6000/ 0.6187×0.6187×0.6200		
CHUV	Siemens/Philips	3	0.4688×0.4688×0.7000	22/3.95	18
BraVa	Siemens	3	0.6187×0.6187×0.6200	24/4.85	18
IXI-HH	Philips	3	0.4688×0.4688×0.8000	16.7/5.75	16
IXI-IOP	GE	1.5	0.2637×0.2637×0.8000		
IXI-Guys	Philips	1.5	0.4688×0.4688×0.8000		25
MIDAS	Siemens	3	0.5134×0.5134×0.8000		22
MSC	Siemens	3	0.6250×0.6250×1.0000	25/3.34	20
OASIS3	Siemens	3	0.2995×0.2995×0.6000		

After preprocessing, 67 additional datasets were deleted due to data quality problems. The images of these datasets contained severe artifacts that obscured the details of the blood vessels. These artifacts not only degraded the image quality but also compromised the accuracy and reliability of the subsequent analysis. Table 1 describes the demographic information of the remaining 1,336 datasets used to generate the atlases.

To utilize a more diverse set of datasets, those used in this study include various field strengths (1.5T and 3T), scanner types (Siemens and Philips), and acquisition parameters. The scanning parameters related to TOF-MRA are given in Table 2.

PRE-PROCESSING

In the first step of the preprocessing stage, skull stripping, denoising, and bias field correction are performed on MRA images. The BET function (Smith *et al.*, 2002) in FSL 6.0 was used to remove non-brain tissue from the human subjects' images. This preprocessing step is essential for enhancing the accuracy and reliability of subsequent analyses by eliminating potential noise and artifacts from non-brain regions. After skull removal, the images were carefully examined and, if necessary, manually edited using ITK-SNAP. Afterward, the DenoiseImage and N4BiasFieldCorrection functions in ANTs were used for denoising and bias field correction. To reduce the variability of the intensity distribution between scanners and subjects, histogram specification was used to normalize the images. Histogram specification is a technique employed to adjust the global contrast of an image by aligning its histogram with a target histogram. Before applying histogram specification, the input intracranial TOF-MRA data were convolved with a 3×3×3 Gaussian kernel to enhance the continuity of grayscale values, as detailed in the reference (Zhang *et al.*, 2019).

In the second step, the FFCM-MRF (Cui *et al.*, 2024) method is used to segment blood vessels in the human dataset. Fast fuzzy c-means (FFCM) clustering is used for rough segmentation of blood vessels. Unlike traditional FCM, the FFCM is based on histograms rather than individual pixels to calculate the membership matrix and clustering center, thereby reducing the execution time of clustering. Due to noise in the coarse segmentation results, it is impossible to capture the vascular structure in low-contrast regions of the image. Therefore, it is necessary to construct the MRF model to further optimize the coarse segmentation results.

In the third step, the 3D centerline representation of each segmentation is calculated by Lee *et al.* (Lee *et al.*, 1994). Next, the distance transform described by Danielsson (Danielsson *et al.*, 1994) is used to calculate the distance from each centerline voxel to the nearest non-vascular voxel, to define the radius of each centerline voxel. Then, a second distance transform is used to identify the nearest centerline voxel for each voxel within 6 mm of the centerline voxel. In this way, the radius value of the centerline voxel determined by the first distance transform is assigned to all non-centerline voxels that are closest to the centerline voxel and within 6 mm. At the same time, the binary image of blood vessel segmentation is used to calculate the distance from the tissue to the blood vessel. The binary image is inverted, with blood vessels marked as 0 and the background as 1. The distance from all voxels marked as 1 to the nearest 0 voxel is then calculated.

In the last step, each TOF MRA image, along with the corresponding blood vessel segmentation image, blood vessel radius image, and the distance image from the tissue to the blood vessel, was registered to the human standard space. The MNI (Mazziotta *et al.*, 2001) brain atlas with a resolution of 0.5 mm^3 was obtained. To generate a statistical atlas, the intensity-normalized TOF MRA atlas, corresponding vascular probability atlas, average radius, standard deviation atlas, and tissue-to-vessel distance atlas were all normalized to a common space.

The registration process is divided into two steps. The first step is to register the T1-weighted image, including the skull, to the corresponding TOF MRA image. Using image registration with the skull reduces the workload of skull removal and ensures consistent brain volume between the two images. Since the two images are from the same individual, a rigid transformation is used. The second step is to register the skull-stripped T1-weighted image from the TOFMRA space to the brain atlas in the standard space using nonlinear registration.ANTs (Avants *et al.*, 2001) with default parameters is used to complete the registration. For a small number of subjects without T1-weighted images, the TOF MRA was directly non-linearly registered to the MNI template. Finally, using the registration file from the second step, the TOF MRA image and the related vascular image are directly transformed to the standard space. Nearest neighbor interpolation is used to register the blood vessel segmentation image and the radius image to the standard space, while the intensity-normalized TOF MRA image is transformed to the atlas space using linear interpolation.

A total of five atlases were generated using the registered images: the TOF MRA intensity atlas, the vascular probability atlas representing the regions, the mean radius of the blood vessels, the standard deviation of the

blood vessel radius, and the corresponding statistical atlas of the distance from the tissue to the blood vessels (Fig. 2).

ATLAS GENERATION

The average intensity atlas of TOF MRA was constructed using the registered TOF MRA images. The voxel intensity in the atlas represents the average intensity of all the corresponding voxel positions after registration. Because the brain volume varies at different sites, a brain mask is used to limit the range of calculation to eliminate this influence. The distance atlas from tissue to blood vessel is also obtained using the same method.

The probability atlas of blood vessels is generated from the segmented images after registration. The atlas represents the probability of blood vessels at each voxel position. Due to the varying brain volumes at different sites, TOF MRA scanning must be considered when calculating the probability of blood vessels. If the intensity value of TOF MRA is 0, the image is excluded from the probability calculation at that voxel position to prevent erroneous probability values.

Finally, the average vascular radius and the corresponding standard deviation at each voxel position are calculated using the registered arterial radius images. When calculating the vascular radius, the brain volumes of different images are also taken into account, and only the effective voxel positions are calculated. For a certain voxel position, the average of all non-zero values is calculated to determine the average vascular radius atlas for each voxel position. Finally, the standard deviation atlas of the vascular radius is calculated using the registered individual radius images and the average vascular radius atlas.

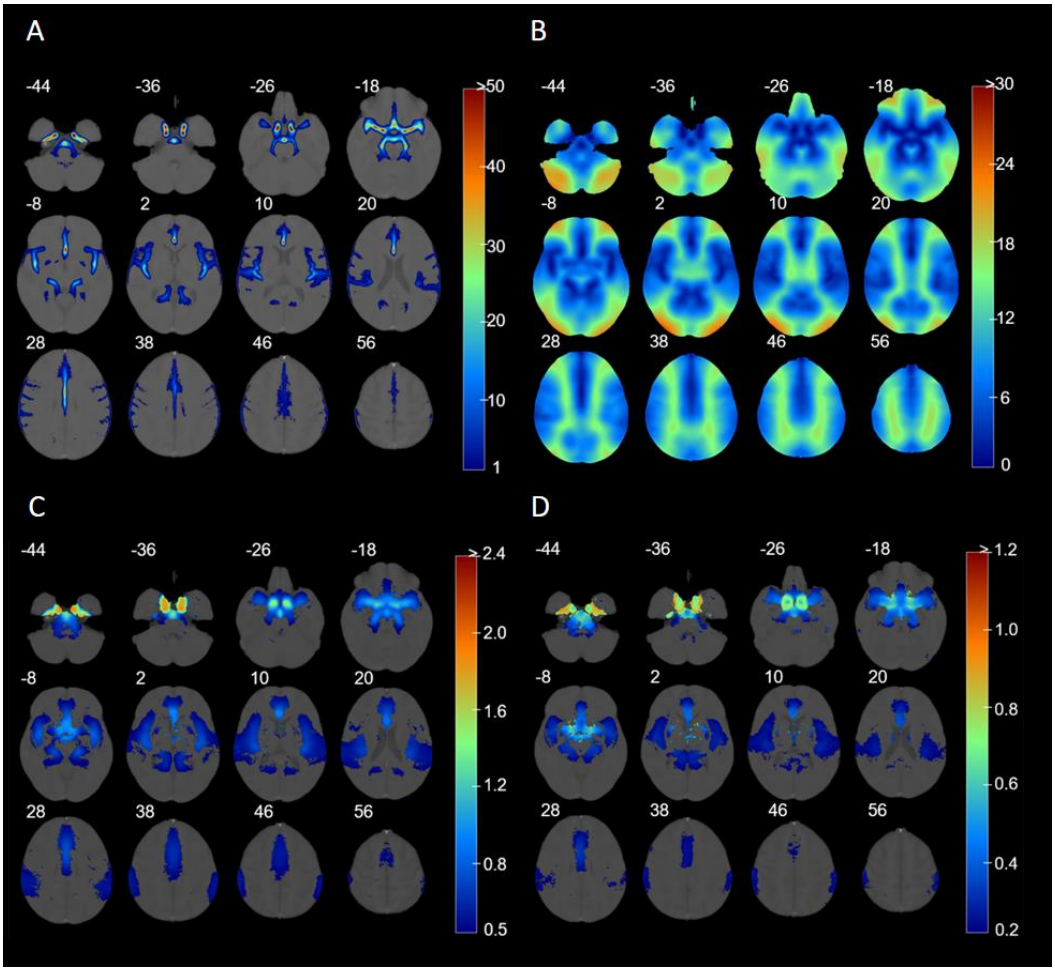

Fig. 2. *Cerebroarterial statistical atlas. Selected slices from the artery probability atlas (A), the mean tissue-to-vessel distance (B), the mean artery radius atlas (C), and the standard deviation atlas (D) overlaid on the time-of-flight (TOF) MRA average atlas. The artery probabilities are presented as percentages, while the mean radius and its standard deviation are shown in millimeters (mm).*

RESULTS

ANALYSIS OF STATISTICAL ATLAS

Visual and quantitative inspections of the generated atlas were performed. The atlas illustrated the major arteries (Fig. 2), indicating a higher probability of their presence. The probability of artery presence diminished as the vessel radius decreased, which aligns with previous research findings (Forkert *et al.*, 2013).

A quantitative analysis was performed on a specific region of interest, namely the vascular segment of the Circle of Willis. The highest probability was observed in the internal carotid artery (ICA), which reached 76%, with an average vessel radius of 1.9 mm. Due to variations in multi-site imaging conditions, the graph does not include the lower segment of the ICA. This measurement falls within the previously reported range of 1.25 to 3.5 mm by Saeki and Rhoton (Saeki & Rhoton, 1977).

The internal carotid artery bifurcates into the middle cerebral artery (MCA) and the anterior cerebral artery (ACA). The average radius of the middle cerebral artery is approximately 1 mm, with a probability of 47%, as indicated in the probability atlas. In contrast, the average radius of the anterior cerebral artery is approximately 0.8 mm, with a probability of 50% in the same atlas. Previous studies have reported that the radius of the anterior cerebral artery ranges from 0.45 mm to 2 mm (Perlmutter *et al.*, 1976).

The basilar artery (BA) primarily serves the posterior circulation of the brain and bifurcates into the posterior cerebral artery (PCA). The probability of occurrence of the basilar artery is as high as 44%, with an average radius of 1.41 mm. Previous studies by Smoker *et al.* (1986) indicated a radius range for the BA of 0.8 mm to 3 mm. The average radius of the posterior cerebral artery (PCA) is approximately 0.65 mm, with a probability as high as 50% in the probability atlas. Previous studies reported a radius range for the P1 segment between 0.4 mm and 1.9 mm (Zeal *et al.*, 1978). The average distance map from tissue to vessels can effectively show the location of vessel distribution. When the distance from tissue to vessels is short, it indicates a high density of vessels in that area.

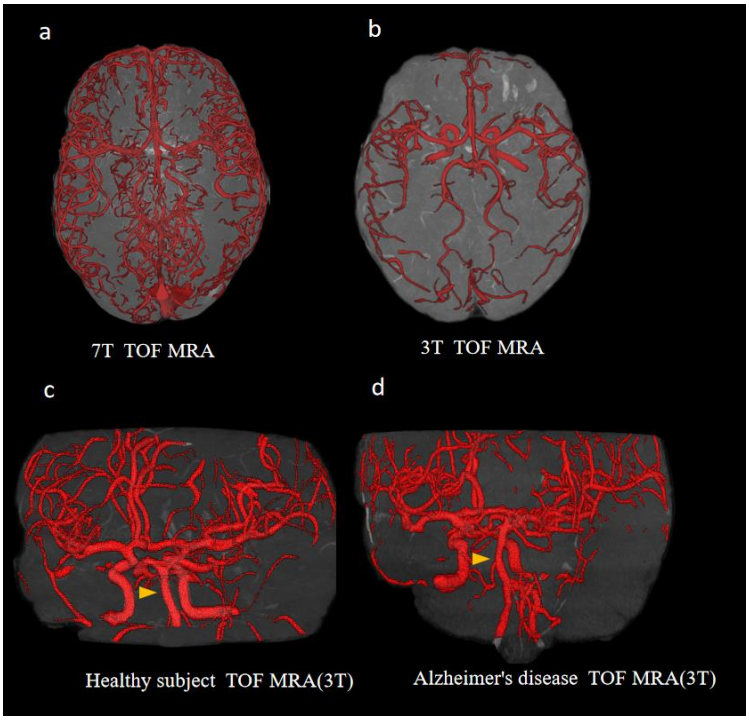

Fig. 3. *Comparison of vascular morphology in 3T, 7T, and Alzheimer's Disease (AD) images.*

DSC BETWEEN SEGMENTED VESSELS AND PROBABILITY ATLASES

The vessel probability atlas, used to represent the probability of vascular structures (Passat *et al.*, 2005), can assist in vessel segmentation, aiding in the identification and extraction of vascular structures within images. To verify the practicality of the generated probability atlas compared to previous ones, vessel segmentation images from 20 subjects using 3T, AD, and 7T (Fig.

3) were utilized to assess the similarity between the vessel segmentation images and the vascular probability atlas. The 3T images are sourced from the ICBM, IXI, and OASIS3 datasets (which do not involve additional datasets for atlas generation), while the 7T images are obtained from the Forrest dataset (https://www.studyforrest.org). Compared to low-field strength magnetic resonance imaging, 7T MRI (Özütemiz *et al.*, 2024) shows significant improvements in resolution, sensitivity, signal quality, and precise diagnostic imaging, allowing for better visualization of distal large arteries and small vascular branches (Sun *et al.*, 2022). The artery probability atlas (2019) and the artery probability atlas generated in this study were registered to individual images, and the similarity between the individual vessel segmentation images and the two vascular probability atlases was calculated.

As shown in Table 3, for both 3T and higher-resolution 7T images, the artery probability atlas (2024) exhibits higher Dice similarity coefficients, indicating that this vascular probability map contains richer and more comprehensive vascular information. It can better generalize to different individual images, making it more suitable for vascular segmentation tasks. In the 3T images, cases 5 and 6 are from AD data, where vascular images of elderly individuals with AD tend to be more tortuous and irregular. However, the Dice similarity coefficient for the artery probability atlas (2024) for these individuals can reach as high as 0.9092, demonstrating that this probability atlas remains stable even when facing complex vascular structures.

Table 3. *Compare the DSC between individual and different probability atlas*

Magnetic field strength	Subject number	DSC(2019)	DSC(2024)
3T	1	0.8951	0.9488
	2	0.9040	0.9422
	3	0.8876	0.9675
	4	0.9130	0.9659
	5	0.8500	0.9092
	6	0.7710	0.8625
7T	7	0.7847	0.8388
	8	0.7682	0.8282
	9	0.7896	0.8533
	10	0.8600	0.9204
	11	0.7974	0.8641
	12	0.7647	0.7747
	13	0.7420	0.7981
	14	0.7679	0.8019
	15	0.8114	0.8747
	16	0.7018	0.7519
	17	0.8374	0.8935
	18	0.7847	0.8159
	19	0.7967	0.8554
	20	0.8146	0.8487

RADIUS ERROR BETWEEN INDIVIDUAL IMAGES AND MEAN ARTERY ATLASES

Due to the inherent differences in vascular structures among individuals of varying ages, this study compares the mean artery radius atlas (2019) and the mean artery radius atlas (2024) to assess the errors between them and individual radii. By registering the radius atlases to individual images, as shown in Fig. 4A, we calculated the differences between the individual radius and the corresponding mean radius atlas. A 3T MRA image of an elderly individual was selected for this analysis, with results displayed in Fig. 4B Panels a-c show the error visualization for the mean artery radius atlas (2019), while panels d-f illustrate the error visualization for the mean artery radius atlas (2024). Larger values indicate greater differences in radius at the corresponding voxel positions. Notably, in the ICA region, the values in the right image are significantly smaller, indicating that the mean artery radius atlas (2024) generated in this study aligns better with the morphology and structure of individual vessels, thereby reflecting the average vascular characteristics of the population more accurately.

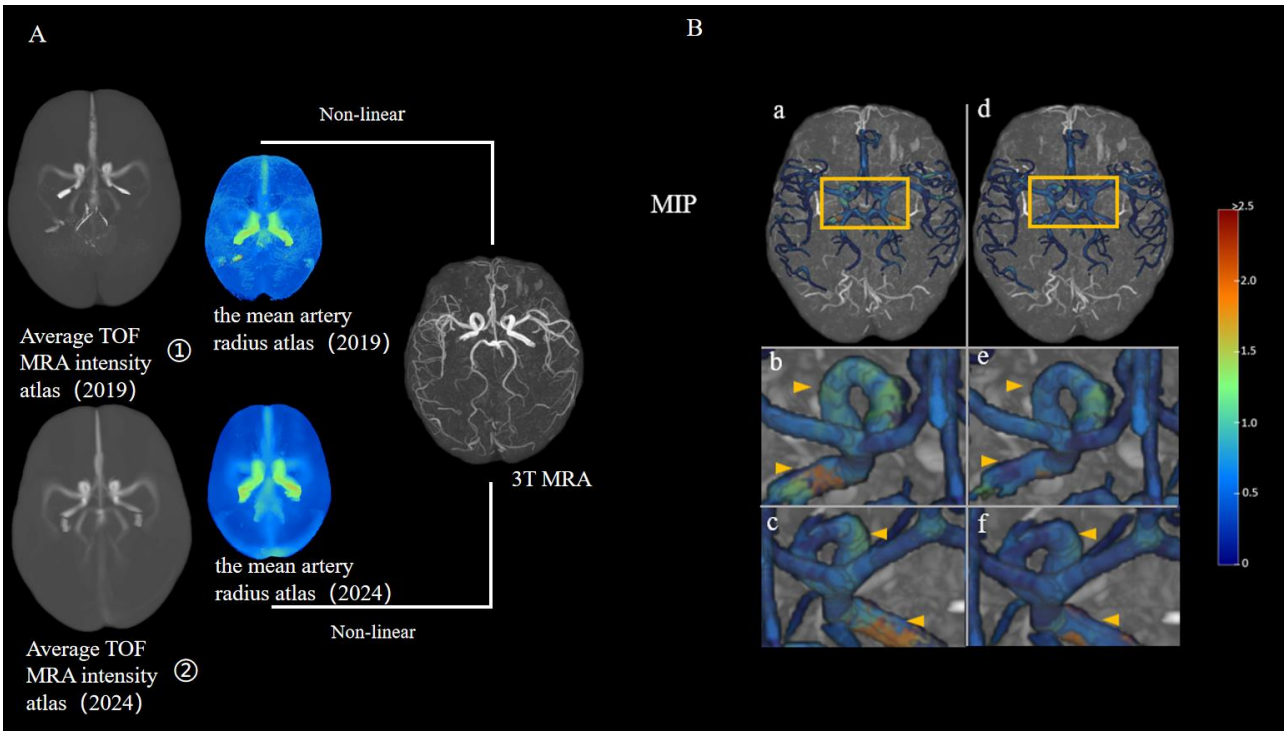

Fig. 4. *Registration Process and Mean Radius* Comparison. (A) Illustrates the process of registering the mean radius atlas to individual subject images. (B) Presents a comparison of differences in artery radii: panels a-c show the discrepancies between the individual artery radius and the mean artery radius atlas from 2019, while panels d-f depict the discrepancies with the updated mean artery radius atlas from 2024. The color scale in each panel indicates the magnitude of radius differences, with warmer colors signifying larger discrepancies.

DISCUSSION

The size, shape, and distribution of individual blood vessels exhibit significant variation among individuals and are influenced by age. In this study, we utilized data from up to 10 sites, employing various field strengths and scanning devices, alongside a diverse age range of 1,336 subjects, to create a more comprehensive vascular statistical atlas.

Notably, the new vascular probability atlas demonstrated higher similarity in the Dice similarity coefficient (DSC) comparison, indicating its applicability across images of different individuals. This characteristic is particularly pronounced in images of elderly patients with Alzheimer's disease (AD), underscoring the stability of the new atlas in handling complex vascular structures.

However, due to discrepancies in scanning, not all datasets sufficiently captured the vessels at the base of the internal carotid artery (ICA), leading to the omission of some segments of these vessels in the generated atlas. Additionally, the current images are derived from 1.5T and 3T scanners, which do not adequately visualize the distal small vascular segments. In the future, incorporating 7T imaging data could enhance the comprehensiveness of the vascular statistical atlas.

In conclusion, this study not only validates the effectiveness of the new vascular probability atlas but also offers valuable insights for future research directions. Subsequent studies could further investigate the differences in vascular characteristics among diverse populations. By incorporating emerging imaging technologies and advanced algorithms, researchers could enhance the accuracy of vascular segmentation, ultimately providing more precise support for clinical applications.

REFERENCES

Avants BB, Tustison N, Song G (2009). Advanced normalization tools (ANTS). Insight J 2(365):1–35.

Cool D, Chillet D, Kim J, Guyon JP, Foskey M, Aylward S (2003). Tissue-based affine registration of brain images to form a vascular density atlas. Med Image Comput Comput Assist Interv 6:9-15.

Cui Y, Huang H, Liu J, Zhao M, Li C, Han X, *et al.* (2024). FFCM-MRF: An accurate and generalizable cerebrovascular segmentation pipeline for humans and rhesus monkeys based on TOF-MRA. Comput Biol Med 170:107996.

Danielsson PE (1980). Euclidean distance mapping. Comput Graph Image Process 14:227–48.

Dunås, T., Wåhlin, A., Ambarki K, Zarrinkoob L, Malm J, Eklund A (2017). A stereotactic probabilistic atlas for the major cerebral arteries. Neuroinformatics 15:101–110.

Dufour A, Tankyevych O, Talbot H, Ronse C (2011). A statistical arteriovenous cerebral atlas. MICCAI Workshop Comput Vis (Intra)Vasc Imaging 73–80.

Forkert ND, Fiehler J, Suniaga S, Wersching H, Knecht S, Kemmling A (2013). A statistical cerebroarterial atlas derived from 700 MRA datasets. Methods Inf Med 52:467–474.

Iadecola C, Gottesman RF (2018). Cerebrovascular alterations in Alzheimer disease: Incidental or pathogenic? Circ Res 123:406–8.

Lee TC, Kashyap RL, Chu CN (1994). Building skeleton models via 3-D medial surface axis thinning algorithms. CVGIP Graph Model Image Process 56:462–78.

Mazziotta J, Toga A, Evans A, Fox P, Lancaster J, Zilles K, Woods R, Mazoyer B (2001). A probabilistic atlas and reference system for the human brain: International Consortium for Brain Mapping (ICBM). Philos Trans R Soc Lond B Biol Sci 356:1293–1322.

Mouches P, Forkert ND (2019). A statistical atlas of cerebral arteries generated using multi-center MRA datasets from healthy subjects. Sci Data 6:29.

Özütemiz C (2024). Cerebrovascular imaging at 7T: A new high. Semin Roentgenol 59:148–56.

Passat N, Ronse C, Baruthio J, Armspach JP, Maillot C (2005). Cerebral vascular atlas generation for anatomical knowledge modeling and segmentation purpose. In: Proc IEEE Conf Comput Vis Pattern Recognit (CVPR) 2:331–7.

Perlmutter D, Rhoton A (1976). Microsurgical anatomy of the anterior cerebral-anterior communicating-recurrent artery complex. J Neurosurg 45:259–72.

Saeki N, Rhoton A (1977). Microsurgical anatomy of the upper basilar artery and the posterior circle of Willis. J Neurosurg 46:563–78.

Smith SM (2002). Fast robust automated brain extraction. Hum Brain Mapp 17:143–55.

Smoker WR, Price MJ, Keyes WD, Corbett JJ and Gentry LR (1986). High-resolution computed tomography of the basilar artery: 1. Normal size and position. AJNR Am J Neuroradiol 7:55-60.

Sun Z, et al. (2022). Age-related tortuosity of carotid and vertebral arteries: Quantitative evaluation with MR angiography. Front Neurol 13:858805.

Zeal AA, Rhoton AL (1978). Microsurgical anatomy of the posterior cerebral artery. J Neurosurg 48:534–59.

Zhang B, Wu Z, Liu S, Zhou S, Li N, Zhao G (2019). A device-independent novel statistical modeling for cerebral TOF-MRA data segmentation. In: Workshop on Clinical Image-Based Procedures. Lect Notes Comput Sci 11840:172–81. Springer.